Repeater-Assisted MIMO Can Also Boost Frequency Diversity: A Semi-Analytic Study

Hiroki Iimori and Yuto Hama
Ericsson Research, Ericsson Japan K.K., Yokohama 220-0012, Japan
(e-mail: {hiroki.iimori, yuto.hama}@ericsson.com)

***Abstract*—Massive multiple-input multiple-output (MIMO) has enabled substantial spatial multiplexing and array gains in real-world systems, while distributed MIMO (D-MIMO) improves macro-diversity over wide areas at the cost of deployment complexity. Repeater-assisted massive MIMO (RA-MIMO) is a lower-cost alternative that can recover key distributed-MIMO advantages. This paper asks whether repeater assistance can also enhance *frequency diversity*. We study an uncoded discrete Fourier transform-spread orthogonal frequency-division multiplexing (DFT-s-OFDM) uplink with one-tap single-carrier frequency-domain equalization (SC-FDE) based on minimum mean-square error (MMSE) and derive a receiver-matched semi-analytic bit error rate (BER) expression by averaging over channel and interference realizations, without Gaussian approximation of residual despreading interference. The analysis clarifies how repeater delay reshapes frequency correlation, and waveform simulations confirm tight agreement with the derived expression together with improved high-signal-to-noise ratio (SNR) BER decay, highlighting delay as a practical tuning knob.**

***Index Terms*—Massive MIMO, distributed MIMO, repeater-assisted MIMO, semi-analytic BER, frequency diversity.**

I. Introduction

Massive multiple-input multiple-output (MIMO) is a cornerstone technology of 5G and beyond cellular systems [1], [2]. In sub-6 GHz time-division duplex (TDD) deployments, reciprocity-based multi-user beamforming enables serving many user equipments (UEs) within the same time–frequency resource while achieving substantial array gain through phase-coherent combining, thereby improving signal quality and link budget. Despite these benefits, co-located massive MIMO may still suffer from coverage holes, and it can be challenging to reliably transmit multiple spatial streams to UEs when the propagation environment does not provide enough independent scatterers to yield sufficient channel rank. Distributed MIMO (D-MIMO), also known as cell-free massive MIMO, has emerged as a promising remedy: by densely deploying access points over a wide area, D-MIMO reduces path loss via shorter access-point-to-UE distances, improves coverage, and mitigates shadow fading through enhanced macro diversity; moreover, favorable multi-path propagation can arise even under line-of-sight conditions [3], [4].

While D-MIMO offers compelling performance opportunities, its realization raises deployment and operational challenges. Key issues include transporting data to distributed units, deciding where processing should take place, synchronizing many access points, and distributing clocks and phase references with the accuracy needed for coherent multi-user downlink transmission; current standards and architectures are largely built around co-located MIMO, making a transition to originally-envisioned D-MIMO costly. Motivated by the desire for smaller, backward-compatible steps toward densification, repeater-assisted massive MIMO (RA-MIMO) deploys many small, inexpensive full-duplex repeaters that receive and retransmit signals instantaneously, thereby acting as *active scatterers* (ordinary channel scatterers but with amplification) [5]. Repeaters have long been used to improve coverage, and prior studies have examined capacity and coverage in repeater-aided MIMO, including outdoor-to-indoor improvements using full-duplex relays [5]. In this paradigm, the base station retains control of multi-antenna processing while the repeaters enrich propagation, potentially narrowing the gap between co-located and distributed MIMO without backhaul or tight phase synchronization among many distributed transmitters.

Existing work on repeater-assisted MIMO spans a broad set of architectures and objectives, including repeater-assisted rate-splitting multiple access (RSMA), integrated sensing and communications with repeater swarms, gain/phase optimization, dynamic-TDD operation, full-duplex processing, activation control, and reciprocity calibration [6]–[16]. These studies report gains such as improved ergodic rate and fairness, better sensing performance under communication constraints, and behavior closer to distributed-MIMO without fronthaul. However, evaluations have focused mainly on spatial-domain metrics (coverage, spectral efficiency, signal-to-interference-plus-noise ratio (SINR) uniformity, and interference management), while the effect of repeater assistance on frequency-domain channel structure and diversity remains comparatively underexplored. Since repeater-induced links add delayed and amplified components, they can reshape the effective impulse response and increase frequency selectivity, motivating the central question of this work: *Can repeater assistance improve not only spatial macro diversity but also frequency diversity?*

To answer this question, this paper develops a receiver-matched analysis and validation framework for a wideband uplink with repeater-assisted propagation. Specifically, we consider an uncoded single-carrier signaling in the framework of the orthogonal frequency-division multiplexing (OFDM) system, which is implemented as discrete Fourier transform-spread orthogonal frequency-division multiplexing (DFT-s-OFDM) with one-tap minimum mean-square error (MMSE) equalization in the frequency domain. We derive a semi-analytic bit error rate (BER) expression by starting from

the symbol-domain equivalent model and then taking the expectation over channel and interference realizations. The main contributions are as follows: 1) we derive a semi-analytic BER framework that preserves the exact structured residual interference term after despreading (without coarse Gaussian approximation); 2) we show analytically how repeater delays reshape frequency correlation through delay-domain PDP shifts; and 3) we validate the analysis against waveform-level Monte Carlo simulations and quantify the resulting high-signal-to-noise ratio (SNR) frequency-diversity gains. These results highlight repeater processing delay as a practical design parameter for reliability improvement.

A. Notation

Scalars are written in plain font (e.g., x, $h_k(\boldsymbol{\tau})$, γ), vectors in bold lowercase (e.g., $\boldsymbol{x}$), and matrices in bold uppercase (e.g., $\mathbf{F}$, $\mathbf{H}$). The operators $(\cdot)^T$, $(\cdot)^H$, and $(\cdot)^*$ denote transpose, Hermitian transpose, and complex conjugate. The real and imaginary parts are $\mathrm{Re}\{\cdot\}$ and $\mathrm{Im}\{\cdot\}$. The symbol $*$ denotes linear convolution, and ℓ denotes the discrete-time tap (delay) index.

II. System Model

This section establishes the baseband system description used throughout the paper. To enable the frequency-diversity analysis and evaluation in later sections, we first present the transmit–receive signal model and its frequency-domain input–output relationship for a representative single-carrier OFDM waveform, using DFT-s-OFDM as a concrete example. We then introduce the channel model, including the direct path and the repeater-induced cascaded components.

A. Input-Output Signal Model

To keep the error rate derivation and evaluation tractable while still exposing the essential frequency-diversity mechanism, we use uncoded DFT-s-OFDM as a representative single-carrier OFDM waveform. In DFT-s-OFDM, discrete Fourier transform (DFT) precoding spreads each data symbol across the allocated subcarriers, and the subsequent IDFT (OFDM modulation) transforms the mapped spectrum back to the time domain. This structure produces a low-PAPR, single-carrier-like transmit waveform while retaining frequency-domain processing and one-tap equalization. As a result of DFT spreading, each data symbol is distributed over frequency and therefore experiences multiple (generally different) channel responses, which enables capturing frequency diversity[1].

Let $M \le N$ be the DFT spreading size and OFDM FFT size. Let $\boldsymbol{x} \in \mathbb{C}^{M\times 1}$ denote data symbols with $\mathbb{E}\{|x_i|^2\} = 1$. The DFT-spread vector is

$$\boldsymbol{x}_f = \mathbf{F}_M \boldsymbol{x}, \tag{1}$$

where $\mathbf{F}_M$ is the unitary M-point DFT matrix.

[1]Channel coding can further exploit this diversity gain, but it complicates the analysis; therefore, coded systems are left for future work.

Let $\mathbf{P} \in \{0,1\}^{N\times M}$ be the subcarrier-allocation matrix. The mapped frequency-domain OFDM vector is $\boldsymbol{z} = \mathbf{P}\boldsymbol{x}_f$ and the N-sample time-domain transmit block is

$$\boldsymbol{s} = \mathbf{F}_N^H \boldsymbol{z} = \mathbf{F}_N^H \mathbf{P} \mathbf{F}_M \boldsymbol{x}. \tag{2}$$

Next, cyclic prefix (CP) insertion and removal are represented by matrices $\mathbf{C}_{\mathrm{cp}}$ and $\mathbf{R}_{\mathrm{cp}}$. With time-domain convolution matrix $\mathbf{H}_t(\boldsymbol{\tau})$,

$$\boldsymbol{r} = \mathbf{R}_{\mathrm{cp}} \mathbf{H}_t(\boldsymbol{\tau}) \mathbf{C}_{\mathrm{cp}} \boldsymbol{s} + \boldsymbol{w}, \tag{3}$$

where $\boldsymbol{w}$ is AWGN before FFT.

After FFT and subcarrier de-mapping,

$$\boldsymbol{y} = \mathbf{P}^T \mathbf{F}_N \boldsymbol{r} = \mathbf{H}(\boldsymbol{\tau}) \boldsymbol{x}_f + \boldsymbol{n}, \tag{4}$$

where $\mathbf{H}(\boldsymbol{\tau}) = \mathrm{diag}(h_0(\boldsymbol{\tau}), \ldots, h_{M-1}(\boldsymbol{\tau}))$ and $\boldsymbol{n} \sim \mathcal{CN}(\mathbf{0}, \sigma_n^2 \mathbf{I}_M)$, assuming the CP is longer than the effective channel impulse response so that inter-sample interference is avoided and the linear convolution is circular over the N-point block. Equation (4) is the exact receiver-domain starting point used in the BER derivation.

B. Repeater-Assisted Equivalent Channel

This subsection describes how the effective channel is constructed when multiple repeaters assist the link. We analyze one equivalent data stream after spatial processing in a repeater-assisted massive-MIMO uplink, assuming perfect inter-layer/user interference cancellation[2]. Thus, the present model should be interpreted as a post-spatial-processing link abstraction; residual multi-user or multi-layer interference under practical spatial equalization is an important extension rather than part of the present single-stream study. This stream is modeled as a DFT-s-OFDM link over an effective discrete-time channel. Let R denote the number of repeaters. For repeater $r \in \{1, \ldots, R\}$, let $h_{UR,r}[\ell]$ and $h_{RG,r}[\ell]$ denote the discrete-time impulse responses of the UE→repeater and repeater→gNB channels, respectively. The end-to-end cascaded impulse response associated with repeater r is obtained by convolving the two links,

$$h_{c,r}[\ell] = \sum_m h_{UR,r}[m]\, h_{RG,r}[\ell - m] \triangleq (h_{UR,r} * h_{RG,r})[\ell], \tag{5}$$

which indicates that each repeater contributes one convolutional two-hop branch.

Let $h_d[\ell]$ denote the direct UE→gNB impulse response, and let repeater r introduce a processing delay τ_r measured in integer samples. Defining the delay vector $\boldsymbol{\tau} = [\tau_1, \ldots, \tau_R]^T$, and denoting the real nonnegative repeater gain of branch r by g_r, the overall equivalent impulse response seen at the receiver is the superposition of the direct and delayed cascaded components,

$$h[\ell; \boldsymbol{\tau}] = \alpha \left(h_d[\ell] + \sum_{r=1}^{R} g_r h_{c,r}[\ell - \tau_r] \right), \tag{6}$$

[2]With large arrays, conventional MMSE spatial equalization can suppress interference to a large extent. Extensions to a full MIMO setup are left for future work.

with $\alpha = \frac{1}{\sqrt{1+\sum_{r=1}^{R} g_r^2}}$, which normalizes the average channel energy, so adding repeater branches does not increase the average received channel power when the direct and each cascaded branch are individually unit-power on average.

This equivalent discrete-time channel is the impulse response experienced by the DFT-s-OFDM waveform after propagation through all branches. To connect the time-domain representation to the per-subcarrier model, the first N samples are stacked into the length-N vector

$$\boldsymbol{h}(\boldsymbol{\tau}) = \big[h[0;\boldsymbol{\tau}],\, \ldots,\, h[N-1;\boldsymbol{\tau}]\big]^T, \tag{7}$$

with implicit zero-padding beyond the channel support and its N-point DFT being then defined as

$$\boldsymbol{h}_f(\boldsymbol{\tau}) = \mathbf{F}_N \boldsymbol{h}(\boldsymbol{\tau}) \in \mathbb{C}^{N\times 1}. \tag{8}$$

Using the DFT time-shift property, a delay of τ_r samples in time produces a multiplicative phase term $e^{-j2\pi k\tau_r/N}$ on the kth subcarrier. Define the per-subcarrier composite channel coefficient as $h_k(\boldsymbol{\tau}) \triangleq [\boldsymbol{h}_f(\boldsymbol{\tau})]_k$. Let $h_{d,k}$ and $h_{c,r,k}$ denote the corresponding N-point DFT coefficients of $h_d[\ell]$ and $h_{c,r}[\ell]$. Then, for $k = 0, \ldots, N-1$,

$$h_k(\boldsymbol{\tau}) = \alpha \left(h_{d,k} + \sum_{r=1}^{R} g_r e^{-j2\pi k\tau_r/N}\, h_{c,r,k} \right). \tag{9}$$

This expression shows that each repeater delay introduces a deterministic linear phase rotation across subcarriers, thereby modifying the coherent frequency-domain combining of the direct and repeater-assisted branches.

III. Semi-Analytic BER Expression

A. Delay-Domain PDP and Subcarrier Correlation

To provide intuition for why repeater delays can change frequency diversity, we briefly relate the composite impulse response in (6) to its frequency correlation. Define the branch-average power delay profiles (PDPs)

$$p_d[\ell] = \mathbb{E}\{|h_d[\ell]|^2\}, \qquad p_{c,r}[\ell] = \mathbb{E}\{|h_{c,r}[\ell]|^2\}, \tag{10}$$

and, assuming zero-mean taps and statistical independence across the direct and cascaded branches, the equivalent average PDP

$$p_h[\ell;\boldsymbol{\tau}] = \alpha^2 \left(p_d[\ell] + \sum_{r=1}^{R} g_r^2 p_{c,r}[\ell - \tau_r] \right), \tag{11}$$

which indicates that repeater delays shift the corresponding cascaded PDPs in the delay domain while preserving their average power. The factors g_r^2 and α^2 make explicit that delay changes the location of PDP energy, while the total average channel power is kept fixed across direct-only and repeater-assisted configurations.

To characterize frequency selectivity, define the frequency-domain channel correlation function as the subcarrier autocorrelation

$$R_H[\Delta k;\boldsymbol{\tau}] \triangleq \mathbb{E}\big\{h_k(\boldsymbol{\tau}) h_{k+\Delta k}^*(\boldsymbol{\tau})\big\}. \tag{12}$$

Under the wide-sense stationary uncorrelated scattering (WSSUS) assumption, taps at different delays are uncorrelated and the correlation reduces to the DFT of the PDP,

$$R_H[\Delta k;\boldsymbol{\tau}] = \sum_{\ell} p_h[\ell;\boldsymbol{\tau}] e^{-j2\pi\Delta k\ell/N}. \tag{13}$$

Equations (11)-(13) highlight the key mechanism: by shifting energy in delay, $\boldsymbol{\tau}$ changes subcarrier correlation and therefore the amount of frequency diversity that can be extracted after equalization and despreading.

B. MMSE Equalization and Despreading

This subsection derives the symbol-domain detector output after applying one-tap MMSE equalization in the frequency domain and then performing IDFT despreading. The result is a compact expression that separates the desired symbol term from the residual inter-symbol interference created by non-flat equalized gains across subcarriers, plus the transformed noise. These expressions set up the exact decomposition needed to compute the conditional error probability in the next step, leading directly to (20)–(18) and then to (16).

The one-tap MMSE coefficient on the kth frequency-domain sample is

$$w_k = \frac{h_k(\boldsymbol{\tau})^*}{|h_k(\boldsymbol{\tau})|^2 + \sigma_n^2}, \tag{14}$$

where noise amplification is suppressed by the denominator; at high SNR and strong channel gain, it approaches zero-forcing behavior; at low SNR or deep fades, it avoids excessive noise enhancement.

Collecting all coefficients in $\mathbf{W} = \mathrm{diag}(w_0, \ldots, w_{M-1})$, the despread output is

$$\hat{\boldsymbol{x}} = \mathbf{F}_M^H \mathbf{W} \boldsymbol{y} = \mathbf{F}_M^H \mathbf{D} \boldsymbol{x}_f + \mathbf{F}_M^H \mathbf{W} \boldsymbol{n}, \tag{15}$$

where $\mathbf{D} = \mathrm{diag}(d_0, \ldots, d_{M-1})$ and $d_k = w_k h_k(\boldsymbol{\tau})$. This equation separates the detector output into an effective linear transformation of symbols and transformed noise.

C. Gain Normalization and Symbol-Domain Decomposition

This subsection converts the frequency-domain equalizer output into a symbol-domain model that is directly usable for BER analysis. We first introduce a scalar gain normalization so that decisions are made at the original constellation scale, and then rewrite the combined MMSE and despreading operation as a circulant linear transformation $\mathbf{C}$ acting on the transmitted symbol vector. Exploiting the circulant structure yields an explicit decomposition of each detected symbol into the desired term, a structured self-interference term I_i, and an effective noise term, which is the key starting point for the conditional error-probability expressions derived next.

To align symbol decisions with the original constellation scale, we normalize by the average real part of the equalized gain

$$g = \frac{1}{M} \sum_{k=0}^{M-1} \mathrm{Re}\{d_k\}, \tag{16}$$

where $d_k = w_k h_k(\boldsymbol{\tau})$ is the MMSE-equalized channel response. For the ideal model in (14), d_k is real-valued; in numerical evaluations, a negligible imaginary part may remain due to finite-precision arithmetic.

Using (16), define

$$\tilde{\boldsymbol{x}} = \frac{1}{g}\hat{\boldsymbol{x}} = \mathbf{C}\boldsymbol{x} + \boldsymbol{\nu}, \quad \mathbf{C} = \frac{1}{g}\mathbf{F}_M^H \mathbf{D} \mathbf{F}_M, \tag{17}$$

$$\boldsymbol{\nu} = \frac{1}{g}\mathbf{F}_M^H \mathbf{W} \boldsymbol{n}. \tag{18}$$

Since $\mathbf{D}$ is diagonal in frequency and surrounded by DFT/IDFT, $\mathbf{C}$ is circulant. Let $\boldsymbol{c} = [c_0, \ldots, c_{M-1}]^T$ be its first column,

$$\boldsymbol{c} = \mathrm{IFFT}\left(\frac{d_0}{g}, \ldots, \frac{d_{M-1}}{g}\right)^T. \tag{19}$$

Then each detected symbol can be written as

$$\tilde{x}_i = x_i + \underbrace{\sum_{m=1}^{M-1} c_m x_{i-m}}_{I_i} + \nu_i, \tag{20}$$

where after equalization and despreading, each symbol equals the desired symbol plus structured finite-dimensional interference plus Gaussian noise.

D. Post-Despread Noise Statistics and Modulation-General BER Form

This subsection completes the probabilistic description of the post-despread detector output by (i) computing the variance of the transformed noise term ν_i after MMSE weighting, IDFT despreading, and gain normalization, and then (ii) expressing the symbol-to-symbol transition probability as an integral over the decision regions. With this, the BER can be written in a modulation-agnostic form conditioned on the structured interference term I_i from (20). This provides the generic BER kernel that we will later average over channel and interference realizations, and it also sets up the QPSK specialization that follows.

From (18),

$$\sigma_\nu^2 = \mathbb{E}\{|\nu_i|^2\} = \frac{\sigma_n^2}{g^2} \cdot \frac{1}{M} \sum_{k=0}^{M-1} |w_k|^2. \tag{21}$$

For a generic modulation alphabet $\mathcal{S}$ with $|\mathcal{S}| = M_c$ and $m_b = \log_2 M_c$ bits/symbol, define the bit-labeling map $\lambda : \mathcal{S} \to \{0,1\}^{m_b}$ and decision region $\mathcal{R}_{\hat{s}}$ for each $\hat{s} \in \mathcal{S}$. Conditioned on I_i and transmitted symbol $s \in \mathcal{S}$, the transition probability is

$$P(\hat{s} \mid s, I_i) = \iint_{z \in \mathcal{R}_{\hat{s}}} \frac{1}{\pi\sigma_\nu^2} \exp\left(-\frac{|z - (s + I_i)|^2}{\sigma_\nu^2}\right) dz. \tag{22}$$

The conditional BER for arbitrary modulation is then

$$P_{b|I_i}^{(\mathcal{S})} = \frac{1}{m_b M_c} \sum_{s \in \mathcal{S}} \sum_{\hat{s} \in \mathcal{S}} d_H(\lambda(s), \lambda(\hat{s}))\, P(\hat{s} \mid s, I_i), \tag{23}$$

where $d_H(\cdot,\cdot)$ is Hamming distance, and equations (22)–(23) provide a modulation-agnostic semi-analytic BER core.

E. QPSK Example

For Gray-QPSK, each real component takes values $\pm a$ with $a = 1/\sqrt{2}$, and the post-despread noise in each real dimension has variance $\sigma_r^2 = \sigma_\nu^2/2$. Applying the generic decision-region expression in (23) to the model $\hat{x}_i = x_i + I_i + \nu_i$, and averaging over the two equiprobable signs in the in-phase and quadrature dimensions, gives the conditional BER

$$\begin{aligned} P_{b|I_i} = \frac{1}{4}\Bigg[& Q\left(\frac{a + \mathrm{Re}\{I_i\}}{\sigma_r}\right) + Q\left(\frac{a - \mathrm{Re}\{I_i\}}{\sigma_r}\right) \\ & + Q\left(\frac{a + \mathrm{Im}\{I_i\}}{\sigma_r}\right) + Q\left(\frac{a - \mathrm{Im}\{I_i\}}{\sigma_r}\right)\Bigg]. \end{aligned} \tag{24}$$

Other constellations can be treated by retaining (22)–(23) and changing only the decision regions and bit labeling.

F. Final Semi-Analytic BER and Practical Estimator

Since deriving the distribution of I_i is generally challenging, and the expectation over I_i is also difficult because the elements of $\boldsymbol{c}$ are correlated in practice, we resort to a semi-analytic BER expression as follows. The BER at SNR γ and repeater delay setting $\boldsymbol{\tau}$ is the expectation over channel randomness and interfering symbols:

$$\bar{P}_b(\gamma, \boldsymbol{\tau}) = \mathbb{E}_{\boldsymbol{h}(\boldsymbol{\tau})}\Big[\mathbb{E}_{\{x_j\}_{j \neq i}}\Big[P_{b|I_i}^{(\mathcal{S})} \mid \boldsymbol{h}(\boldsymbol{\tau})\Big]\Big]. \tag{25}$$

If the QPSK specialization is used as exemplified in the previous subsection, $P_{b|I_i}^{(\mathcal{S})}$ is replaced by (24). The term "semi-analytic" means the inner probability is analytical, while outer expectations are evaluated numerically.

To elaborate further, with N_B batches, N_H channel realizations per batch, and N_S interference draws per channel,

$$\hat{P}_b(\gamma, \boldsymbol{\tau}) = \frac{1}{N_B} \sum_{b=1}^{N_B} \frac{1}{N_H} \sum_{\ell=1}^{N_H} \frac{1}{N_S} \sum_{q=1}^{N_S} P_{b|I_i^{(b,\ell,q)}}^{(\mathcal{S})}, \tag{26}$$

which is the exact implementation counterpart of (25); thus, analytical structure and simulation procedure are tightly aligned as shown in the simulation result section.

IV. Simulation Results

This section evaluates BER and diversity performance of DFT-s-OFDM over equal-PDP Rayleigh fading using both waveform-level Monte Carlo simulation (full-stack) and a semi-analytic BER evaluation. Three channel configurations are considered: direct transmission only, direct plus one cascaded repeater branch, and direct plus two cascaded repeater branches with different processing delays. For each realization, the effective channel follows the superposition model in (6) and (9). The same average channel-power normalization in (6) is applied to all repeater-assisted cases, so the comparison isolates delay-induced frequency-selectivity effects rather than increased average received energy. The full-stack receiver applies frequency-domain MMSE equalization after CP removal and FFT, followed by IDFT despreading and QPSK demodulation. The semi-analytic BER is evaluated by averaging the conditional BER over channel and interference samples. To numerically capture how increased frequency diversity affects

TABLE I
SIMULATION SETUP

Item	Setting
Waveform	DFT-s-OFDM
FFT size N	128
DFT size M	72
CP length	32
Modulation	QPSK ($M_{\mathrm{QAM}} = 4$)
Full-stack SNR grid	0:1:25 dB
Semi-analytic SNR grid	0:1:45 dB
Full-stack realizations per SNR	100,000
Direct channel taps	$L_{\mathrm{d}} = 4$ (equal PDP Rayleigh)
Repeater UE→R taps	$L_{\mathrm{UR}} = 6$ (equal PDP Rayleigh)
Repeater R→gNB taps	$L_{\mathrm{RG}} = 6$ (equal PDP Rayleigh)
Repeater-1 delay / gain	$d_1 = 8$, $g_1 = 1.0$
Repeater-2 delay / gain	$d_2 = 14$, $g_2 = 1.0$
Maximum effective tap index	$24 < 32$ (within CP)
Transmission block	One OFDM symbol with CP
Semi channel realizations per SNR	3×10^7
Semi interference samples	1000
Semi channel chunk size	700

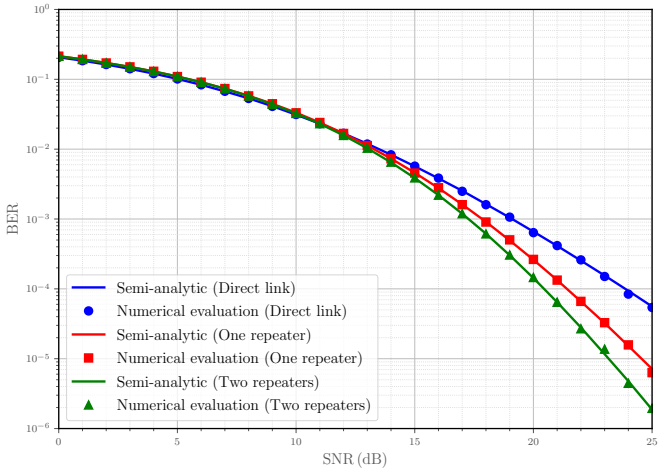


Fig. 1. BER comparison between the proposed semi-analytic evaluation and full-stack waveform Monte Carlo simulation.

high-SNR BER decay, we compute the finite-SNR effective diversity metric directly from BER as

$$d(\gamma) \triangleq -\frac{\log P_e(\gamma)}{\log \gamma}, \tag{27}$$

where γ denotes linear SNR and the formal asymptotic diversity order is theoretically defined only in the limit $\gamma \to \infty$. Thus, $d(\gamma)$ at finite SNR should be interpreted as an operating-point BER exponent, not as a rigorous asymptotic order.

Table I summarizes the simulation configuration. We use FFT size $N = 128$, DFT spreading size $M = 72$, and CP length 32 with QPSK modulation. Here, we consider localized subcarrier allocation as in 5G NR, and we assume $\mathbf{P} = [\mathbf{I}_M,\ \mathbf{O}_{(N-M)\times M}]^{\mathrm{T}}$. BER is computed on two SNR grids: 0:1:25 dB for full-stack simulation and 0:1:45 dB for semi-analytic evaluation. The direct channel uses $L_{\mathrm{d}} = 4$ equal-PDP Rayleigh taps, and each cascaded branch uses $L_{\mathrm{UR}} = 6$ and $L_{\mathrm{RG}} = 6$ taps with repeater settings $(d_1, g_1) = (8, 1.0)$ and $(d_2, g_2) = (14, 1.0)$. These illustrative, delay-separated settings move cascaded PDP energy away from the direct path and reduce subcarrier correlation while remaining within the CP; they are not claimed to be optimal. With zero-based tap indexing, the largest two-repeater tap is $d_2 + (L_{\mathrm{UR}} - 1) + (L_{\mathrm{RG}} - 1) = 14 + 5 + 5 = 24 < 32$, so the one-OFDM-symbol evaluation has no neighboring-symbol interference and remains consistent with circular convolution. In the semi-analytic computation, 3×10^7 channel realizations per SNR, 1000 interference samples, and chunk size 700 are used to balance estimator stability and runtime. The numerical parameters are chosen to expose the frequency-diversity mechanism with a compact but non-flat DFT-s-OFDM allocation: QPSK keeps the BER kernel transparent, equal-PDP Rayleigh taps isolate multipath diversity without geometry-specific path-loss assumptions, unit repeater gains combined with (6) enforce fair average channel power, and the extended semi-analytic SNR grid is used to observe the high-SNR trend beyond the practical Monte Carlo error floor.

A. Semi-Analytic and Waveform BER Consistency

Fig. 1 compares BER versus SNR for the direct link, one-repeater link, and two-repeater link, where solid lines denote the semi-analytic results and markers denote full-stack Monte Carlo simulation. The near-overlap between each line-marker pair across the full SNR range validates the semi-analytic formulation as an accurate surrogate for waveform-level simulation. At low SNR, all three configurations are close because noise dominates performance; however, beyond roughly 15 dB, repeater-assisted links show a clear advantage, with the two-repeater case consistently achieving the lowest BER and the steepest high-SNR decay. For example, around 25 dB the BER is reduced from approximately $O(10^{-5})$ for the direct link to approximately $O(10^{-6})$ with one/two repeaters, and at a target BER near 10^{-4} the repeater cases provide an SNR saving of roughly a few dB. These results indicate that adding cascaded repeater branches improves reliability; the numerical metric in Fig. 2 is then used only to summarize the corresponding BER-decay trend.

B. Numerical Effective-Diversity Metric

Fig. 2 shows the numerically evaluated finite-SNR effective diversity metric $d(\gamma) = -\log(P_e)/\log(\gamma)$ for the direct, one-repeater, and two-repeater configurations. In this plot, P_e is taken from the semi-analytic BER curves (rather than full-stack Monte Carlo BER), justified by the close agreement between semi-analytic and full-stack results established in Fig. 1. This quantity is used as a numerical indicator of the BER-decay effect associated with stronger frequency diversity; it is not used as a substitute for a rigorous asymptotic diversity-order derivation. All curves exhibit a similar low-SNR transient, which should not be interpreted as a diversity-order statement. Accordingly, Fig. 2 is used to visualize the finite-SNR BER-decay behavior over the simulated range, not to claim that the exact asymptotic diversity order has been

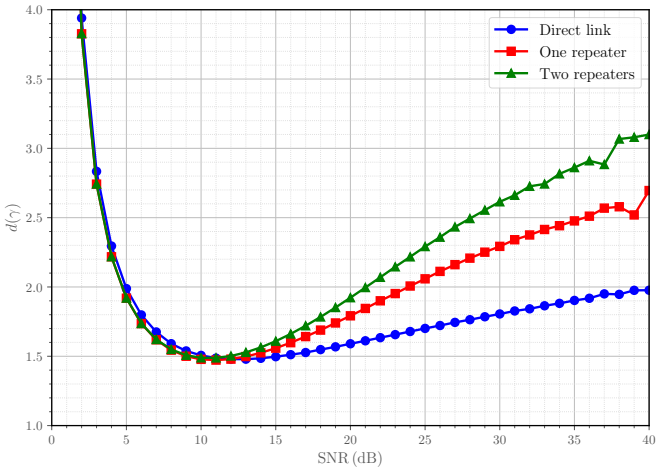


Fig. 2. Finite-SNR effective-diversity metric for the direct-only and repeater-assisted cases.

derived. The curves then settle near $d \approx 1.5$ around the mid-SNR region (roughly 10–12 dB), after which clear separation appears: the direct link increases most slowly, the one-repeater case grows faster, and the two-repeater case achieves the largest value of this slope-equivalent numerical metric at high SNR. By 40 dB, the diversity metric is approximately 2.0 (direct), 2.7 (one repeater), and 3.1 (two repeaters), which is consistent with progressively stronger frequency-diversity behavior from the delayed cascaded branches. The fractional values arise because $d(\gamma)$ is evaluated at finite SNR with MMSE equalization, residual despreading interference, and correlated subcarrier gains; only an asymptotic limit, if derived, would be interpreted as a formal diversity order.

V. Conclusion

This paper investigated repeater-assisted DFT-s-OFDM links over frequency-selective Rayleigh fading using both full-stack waveform simulation and a validated semi-analytic BER framework. The results show that repeater assistance provides not only the well-known spatial/macroscopic coverage benefits but also measurable frequency-diversity gains through delayed cascaded components. Specifically, repeater-assisted configurations achieve lower BER and larger values of the finite-SNR BER-decay metric than the direct link in the high-SNR region, with stronger gains when additional repeater branches are introduced. From an engineering perspective, the gains are most visible once the link enters the medium/high-SNR region where frequency selectivity, rather than noise dominance, governs error decay. The results also suggest that repeater delay planning is not merely an implementation artifact: it directly affects subcarrier correlation and the diversity extracted after MMSE equalization and despreading. An important direction for future work is to quantify how practical constraints affect these gains in realistic deployments. In particular, cyclic-prefix limitations, repeater group delay, repeater noise amplification, and inter-path correlation may reduce, saturate, or even negate the diversity gains observed under idealized assumptions. Timing-offset and carrier-frequency-offset synchronization errors, time-varying channels, imperfect channel estimation, and residual spatial interference in multi-user or multi-layer RA-MIMO are especially relevant for OFDM-based systems and should be incorporated in a more complete analytical and system-level framework. Therefore, system-level evaluation that jointly models physical layer (PHY) processing, synchronization, channel estimation, delay-budget constraints, and network geometry is needed to identify operating regimes where repeater-assisted frequency-diversity gains remain robust.

References

[1] T. L. Marzetta, "Noncooperative cellular wireless with unlimited numbers of base station antennas," *IEEE Trans. Wireless Commun.*, vol. 9, no. 11, pp. 3590–3600, 2010.

[2] E. G. Larsson, O. Edfors, F. Tufvesson, and T. L. Marzetta, "Massive MIMO for next generation wireless systems," *IEEE Commun. Mag.*, vol. 52, no. 2, pp. 186–195, 2014.

[3] H. Q. Ngo, A. Ashikhmin, H. Yang, E. G. Larsson, and T. L. Marzetta, "Cell-free massive MIMO versus small cells," *IEEE Trans. Wireless Commun.*, vol. 16, no. 3, pp. 1834–1850, 2017.

[4] H. A. Ammar, R. Adve, S. Shahbazpanahi, G. Boudreau, and K. V. Srinivas, "User-centric cell-free massive MIMO networks: A survey of opportunities, challenges and solutions," *IEEE Commun. Surv. Tutor.*, vol. 24, no. 1, pp. 611–652, 2022.

[5] S. Willhammar, H. Iimori, J. Vieira, L. Sundström, F. Tufvesson, and E. G. Larsson, "Achieving distributed MIMO performance with repeater-assisted cellular massive MIMO," *IEEE Commun. Mag.*, vol. 63, no. 3, pp. 114–119, Mar. 2025.

[6] T.-H. Vu, N. H. Tu, and V. N. Q. Bao, "Study on reconfigurable repeater-based RSMA systems," *IEEE Wireless Commun. Lett.*, vol. 14, no. 5, pp. 1371–1375, May 2025.

[7] P. Jopanya and D. P. M. Osorio, "Enabling drone detection with swarm repeater-assisted MIMO ISAC," *arXiv preprint arXiv:2509.19119*, Sept. 2025. [Online]. Available: https://arxiv.org/abs/2509.19119

[8] H. Iimori, E. Kurihara, T. Yoshida, J. Vieira, and S. Malomsoky, "Amplification strategy in repeater-assisted MIMO systems via minorization maximization," in *Proc. IEEE Glob. Commun. Conf. (GLOBECOM)*, Kuala Lumpur, Malaysia, Dec. 2023.

[9] M. Andersson, A. Chowdhury, and E. G. Larsson, "Is repeater-assisted massive MIMO compatible with dynamic TDD?" *arXiv preprint arXiv:2510.20998*, Jan. 2026. [Online]. Available: https://arxiv.org/abs/2510.20998

[10] M. Mohammadi, D. Kudathanthirige, H. A. Suraweera, H. Q. Ngo, and M. Matthaiou, "Repeater-assisted massive MIMO full-duplex communications," *arXiv preprint arXiv:2601.20822*, 2026.

[11] O. A. Topal, O. T. Demir, E. Björnson, and C. Cavdar, "Fair and energy-efficient activation control mechanisms for repeater-assisted massive MIMO," *arXiv preprint arXiv:2504.03428*, Apr. 2025. [Online]. Available: https://arxiv.org/abs/2504.03428

[12] A. Chowdhury and E. G. Larsson, "On the performance of dual-antenna repeater assisted bi-static MIMO ISAC," *arXiv preprint arXiv:2511.17980*, Jan. 2026. [Online]. Available: https://arxiv.org/abs/2511.17980

[13] J. Bai, A. Chowdhury, A. Hansson, and E. G. Larsson, "Repeater swarm-assisted cellular systems: Interaction stability and performance analysis," *IEEE Trans. Wireless Commun.*, vol. 25, pp. 10 018–10 034, Jan. 2026.

[14] A.-T. Le, T.-H. Vu, N. H. Tu, T. N. Nguyen, L.-T. Tu, and M. Voznak, "Active-reconfigurable-repeater-assisted NOMA networks in internet of things: Reliability, security, and covertness," *IEEE Internet Things J.*, vol. 12, no. 7, pp. 8759–8772, Apr. 2025.

[15] E. G. Larsson, J. Vieira, and P. Frenger, "Reciprocity calibration of dual-antenna repeaters," *IEEE Wireless Commun. Lett.*, vol. 13, no. 6, pp. 1606–1610, 2024.

[16] S. Hara, T. Takahashi, H. Iimori, H. Ochiai, and E. G. Larsson, "Reciprocity calibration of dual-antenna repeaters via MMSE estimation," *arXiv preprint arXiv:2602.05724*, Feb. 2026. [Online]. Available: https://arxiv.org/abs/2602.05724